In situ measurements of dynamic bacteria transport and attachment in heterogeneous sand-packed columns

Vy Le,* Sophia Thompson, Eric Roden, and Christopher Zahasky

Department of Geoscience, University of Wisconsin-Madison, Madison, Wisconsin 53706, USA

E-mail: vple@wisc.edu

Abstract

Prevention, mitigation, and regulation of bacterial contaminants in groundwater require a fundamental understanding of the mechanisms of transport and attachment in complex geological materials. Discrepancies in bacteria transport behaviors observed between field studies and laboratory experiments indicate an incomplete understanding of dynamic bacteria transport and immobilization processes in realistic heterogeneous geologic systems. Here, we develop a new experimental approach for *in situ* quantification of dynamic bacteria transport and attachment distribution in geologic media that relies on radiolabeling *Escherichia coli* with positron-emitting radioisotopes and quantifying transport with three-dimensional (3D) positron emission tomography (PET) imaging. Our results indicate that the highest bacterial attachment occurred at the interfaces between sand layers oriented orthogonal to the direction of flow. The predicted bacterial attachment from a 3D numerical model matched the experimental PET results, highlighting that experimentally-observed bacteria transport behavior can be accurately captured with a distribution of a first-order irreversible attachment

model. This is the first demonstration of direct measurement of attachment coefficient distributions from bacteria transport experiments in geologic media and provides a transformational approach to better understand bacterial transport mechanisms, improve model parameterization, and accurately predict how local geologic conditions can influence bacterial fate and transport in groundwater.

Keywords

bacteria colloid, column experiment, radioisotope, PET imaging, attachment coefficient, heterogeneity, grain interface

Sypnosis

A new technique using radiolabeled bacteria and PET imaging shows highest bacterial attachment in groundwater occurs at sand layer interfaces. It improves understanding and prediction of bacteria transport in groundwater.

Introduction

Studying the transport and fate of colloidal bacteria in groundwater systems is important for limiting water-borne disease[1,2] and has important implications for the persistence and mobility of other contaminants such as metals in soils,[3] nonaqueous phase liquid biodegradation,[4] and denitrification of groundwater.[5] One of the most common bacteria found in water resources is *Escherichia coli* (*E. coli*). Widespread land application of animal waste containing *E. coli* and other pathogens poses a persistent risk to groundwater systems, especially due to the long-term survival rates of *E. coli* in the subsurface.[6–10] Mitigating these risks requires an improved understanding of bacterial colloid transport and immobilization under complex hydrogeologic conditions.

Similar to colloids, mechanistic descriptions of bacterial transport in porous media are

often adapted from colloid filtration theory (CFT).[11–16] While CFT has been widely applied to quantitatively predict the likelihood of colloids contacting the grain surfaces during transport, it fails to account for reversible colloid attachment, heterogeneous deposition rates (k_f), bacteria straining, pore-size exclusion, and influence of microbial properties such as cell motility and bacterial surface properties. Here, the term bacterial/colloid attachment is used as an encompassing term to describe immobilization of bacteria that can be caused by mechanisms such as electrostatic forces of attraction, steric forces, hydration forces, shear forces, surface topology, etc.[17] Pore size exclusion refers to the inability of colloids to pass through a pore space due to small pore throat-to-colloid size ratio leading to colloids being excluded from certain pores downstream.[18–20] CFT is a mechanistic approach developed at the pore scale to predict the attachment rate coefficient that applies at the continuum scale. However, complexities exist outside the unit collectors underlying CFT, which has driven various approaches to manipulate rate coefficients directly at the continuum scale without mechanistically simulating the pore scale processes such as incorporating multi-rate attachment,[21,22] depth-dependent straining,[19,23] parameters to account for pore size exclusion,[24,25] sorption/retardation-like terms,[26] statistical/stochastic colloid modeling approaches,[26,27] and Lagrangian model frameworks.[28–31]

At the column scale, a key challenge is the unique parameterization of bacteria transport models using traditional experimental data that exhibit spatially-variable attachment coefficients,[32] short and long-term detachment statistics,[26,33] early breakthrough observations,[25,34] and long-tail breakthrough curve behavior.[35,36] Mechanistic simulations of colloid-surface interactions at the pore- and nano-scale have been shown to generate some of these phenomena;[16,37] however, observational linkages between these multi-scale processes remain challenging. Specifically, bacterial effluent concentration measurements have repeatedly been shown to be insufficient for the unique interpretation of colloid attachment, dispersion, and pore water velocity.[22,38,39] Despite this gap, current methods for retention profile determination are laborious, one-dimensional in space, and typically only provide profiles at one

instance in time—at the time of destructive column analysis.[22,40]

Three-dimensional (3D) *in situ* imaging has the potential to provide spatial and temporal bacteria transport and attachment information that is necessary to characterize and understand dynamic and heterogeneous systems. Previous studies have utilized *in situ* approaches including optical imaging of fluorescent colloids in transparent media,[38,41] X-ray micro-computed tomography (X-ray μCT),[42–44] and magnetic resonance imaging.[45,46] However, optical and magnetic resonance imaging approaches are constrained to idealized systems such as glass bead packs or silica gel[46,47] rather than geologic soils and aquifer materials[45,46] and X-ray μCT is constrained to small spatial scales (<1 cm), limiting the applicability of these types of *in situ* measurements in under realistic environmental and geologic conditions. While transport studies of fluorescent bacteria[48–52] have provided valuable insights into the pore-scale deposition and transport mechanisms of *E. coli* in sands, bacteria attachment rates in those studies were inferred from fitting breakthrough curves and in some cases 1D retention profiles and thus were not able to uniquely measure the attachment rate distributions.

Positron emission tomography (PET) is a medical imaging technique that relies on the emission, detection, and reconstruction of high-energy photons from positron-emitting radiolabeled compounds.[53] Tomographic reconstruction methods provide a way to acquire three-dimensional time-lapse images of the radiolabeled compound distribution in geologic materials. Radioisotopes that release high energy photons (511 keV) during positron emission and annihilation events are ideally suited for geologic materials that otherwise cause significant photoelectric adsorption and attenuation of lower energy photons.[54,55] PET imaging thus provides a powerful non-destructive approach for characterizing dynamic *in situ* transport and attachment of bacteria radiolabeled with positron-emitting radioisotopes.

Utilization of PET imaging for quantification of bacteria transport and attachment in column experiments first requires radiolabeling the bacteria with a positron-emitting radioisotope. Bacteria have been radiolabeled using two different approaches—siderophore-derived

chelators[56–61] and a glucose analog uptake.[62] While these approaches are being developed for *in vivo* bacteria imaging in medicine,[63] they have not yet been leveraged to study bacteria transport dynamics in environmental or geologic systems.

In this study, we describe an approach for radiolabeling *E. coli* using [^{18}F]-fluorodeoxyglucose (FDG) that enables three-dimensional time-lapse quantification of bacterial transport in geologic materials with positron emission tomography. Measured attachment rate coefficient (k_f) distributions were used to parameterize a 3D continuum-scale transport model with first-order kinetic attachment. The model results of bacterial attachment in the heterogeneous sand column were compared with the experimental results from PET to evaluate the accuracy of this image-based spatially-resolved k_f quantification approach.

Methods

Three-dimensional image-based quantification of *E. coli* transport and attachment in sand-packed columns requires radiolabeling bacteria with a positron-emitting radioisotope, *in situ* imaging of radiolabeled bacteria with PET, and mathematical interpretation of PET images. To verify attachment measurement accuracy, a deterministic bacteria transport model was constructed based on the calculated transport and attachment distributions.

Radiolabeling methodology

The gram-negative *E. coli* strain P8 (ATCC® BAA-1429), referred to as P8 throughout the remainder of this manuscript, was used in this study because it is a nonpathogenic surrogate bacteria strain for the pathogenic *E. coli* O157:H7.[64–67] Prior to PET imaging, extensive batch radiolabeling experiments were done to optimize the experimental timing and growth conditions that produced the highest and most stable uptake and retention of [^{18}F]-FDG by *E. coli* P8.

Bacteria were radiolabeled by adding [^{18}F]-FDG to a 40 mL culture of bacteria grown

in Luria-Bertani (LB), centrifuging at 10,000 rpm for 12 minutes, washing with phosphate-buffered saline (PBS), and resuspending the bacterial cells in 40 mL of nutrient-free 1 mM NaCl saline solution buffered to a pH range of 6.5 to 7. The bacteria were left to uptake the [^{18}F]-FDG for 15 minutes at room temperature (25°C). After [^{18}F]-FDG uptake, the bacterial solution was centrifuged at 10,000 rpm and washed with PBS to remove excess aqueous phase [^{18}F]-FDG in the supernatant. In the batch experiments, the excess [^{18}F]-FDG in the supernatant was monitored as a function of time for up to three hours. Additional details of the radiolabeling and batch study verification workflows are provided in the Supporting Information (SI).

For the PET imaging experiments, the target concentration of [^{18}F]-FDG in the injected bacterial suspension was 1-1.5 mCi/ml. Our previous work found that this level of radioactivity produces the highest signal-to-noise images without saturating the PET scanner.[55] To reach this optimal radio-concentration, the initial bacterial suspension was concentrated to a smaller volume after the uptake procedure, knowing the radiolabel uptake and retention percentages from batch experiments, the initial radionuclide activity (in mCi) from a dose calibration chamber, and the decay rate of ^{18}F. After concentrating the radiolabeled P8 to achieve the ideal concentration, the bacterial suspension was ready for injection into the sand column. The final cell suspension was confirmed to be stable in a separate parallel experiment through time-course optical density measurements and details are provided in the SI Section 5.

PET imaging column experiments

To quantify spatial and temporal distributions of solute and bacteria in sand-packed columns, both conservative solute tracer ([^{18}F]-FDG) and radiolabeled bacteria pulse injection experiments were imaged with PET. Sands collected from Adams County, Wisconsin were separated into two portions through dry sieving, a coarser portion (355-595 μm sieves) and a finer portion (<355 μm sieve). The coarser sand (M356 sand) and finer sand (M324 sand)

with grain size modes of 356 μm and 324 μm, respectively, were wet-packed inside a column into layers perpendicular to the long axis of the flow in the order of M356, M324, and M356 from inlet to outlet as shown in Figure 1. The Fe(II) oxide content of M324 and M356 sands was found to be 10.7 $\pm 0.4\mu$ mol/g and 13.2$\pm$1.5 μ mol/g, respectively, using dithionite-citrate extraction method. We purposefully packed the columns using these similar sand sizes to examine the extent to which PET imaging can detect minor differences in transport behavior in a system with subtle heterogeneity. The heterogeneous column was connected to an experimental platform with dual-piston continuous-flow pumps and saturated with 1 mM NaCl buffered at pH 6.5-7 with 5 mM $NaHCO_3$ until a steady state was reached at 1.83 ml/min. Further details of column packing and experiment procedures are described in the SI.

The PET experiments involved a pulse injection experiment of 1 mL [^{18}F]-FDG in 1 mM NaCl as a conservative solute tracer and followed by a second pulse injection experiment of 1 mL concentrated radiolabeled *E. coli* P8 suspension in the same saline solution. The radio-concentration of each pulse-injected solution was approximately 1-1.5 mCi/ml. The injected cell concentration was approximately 7.6×10^{10} CFUs based on standard plate counting technique[68] and the pulse duration was equivalent to 0.056 pore volume (PV) (see SI). The entire column was simultaneously and continuously scanned for 60 minutes during the tracer pulse injection experiment, followed by another 60-minute scan of the bacteria experiment with the Siemens Inveon PET scanner. PET image acquisition and reconstruction was performed according to previously established methods.[54,69] The images were coarsened before data analysis as described in the SI. A similar column experiment was also conducted using non-radiolabeled *E. coli* and the attachment coefficient k_f was quantified by fitting the breakthrough curves measured by the UV-Vis spectrophotometer. The attachment coefficients from the PET experiment using radiolabeled bacteria were compared to the fitted k_f from UV-Vis experiment to examine the impact of [^{18}F]-FDG on bacterial cell transport. Radiotracer concentrations in the influent and effluent fluids were also measured. Bacterial

effluent in the later half of the breakthrough curve was discretely sampled. The radioactivity of the aqueous-phase bacterial in the effluent was compared to that of the bulk solution to verify the efficacy of our radiolabeling approach (see SI Section 4). These measurements ensure that the PET imaging was quantifying bacterial transport and not free (unattached) [^{18}F]-FDG.

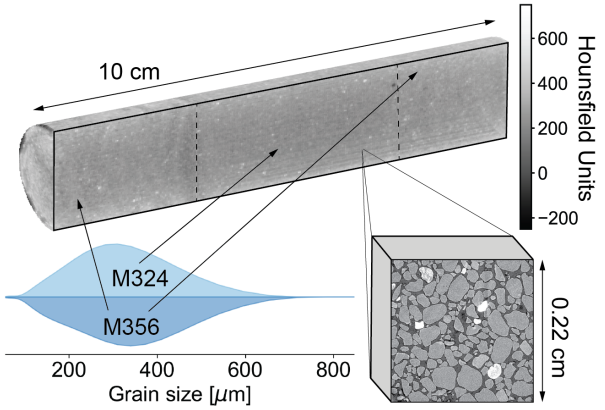

Figure 1: (Top) X-ray computed tomography (CT) image of the heterogeneous column packed with M356 and M324 sands with their respective grain size distributions (lower left). Voxel dimension in the CT image is 0.316 mm x 0.316 mm. (Lower right) Micro-CT image of M356 sand shows the silicate grain matrix (light grey), oxide mineral grains (white), and pore space (darker grey). Each voxel in the micro-CT image is 3.12 μm x 3.12 μm.

Spatially resolved bacterial attachment calculation

The PET scan results provide bacteria breakthrough curves that can be interpreted to quantify transport and attachment information in every 1.553 mm x 1.553 mm x 1.592 mm voxel (n) in the column. The scans throughout the pulse injections provide the total radioactivity concentration in both aqueous and solid phases. Once the aqueous bacteria pulse was displaced out of the column by the non-radioactive background solution, no bacteria were assumed to be in the aqueous phase. At that moment, the observed radioactivity in the PET images represents only the solid-phase attached bacteria concentration.

Calculation of the attachment coefficient in each voxel from the reconstructed PET image is derived from the advection-dispersion equation with a first-order attachment term (see

derivations in SI Section 5). This calculation of k_f requires measurements of the solid-phase attached bacterial concentration S^*/C_0 and integration of the bacterial breakthrough curve (C/C_0) to be evaluated numerically using the composite trapezoidal rule (see SI, Equation 4). Both the voxel-scale attached bacterial concentration and breakthrough curves were obtained from PET imaging data. Boundaries between layers in the column were identified based on the known mass fractions of the packed sand layers. The attached bacterial fraction (S^*/C_0) and the calculated k_f were grouped accordingly based on the voxel locations within these layers for comparison between the sand layers. However, the values of S^*/C_0 and k_f in the first and last voxels in the columns along the z-direction (distance slice) were both excluded so as not to include partial volume artifacts near the inlet and outlet end caps. Image data and scripts used for image analysis and attachment coefficient calculation are provided in the repository referenced in the Acknowledgements.

Three-dimensional first-order bacteria transport model

Results from PET experiments were used for parameterizing a three-dimensional numerical model of the bacterial transport and attachment behavior observed in the column experiments. The model was constructed in MODFLOW 2005[70] and MT3DMS[71] using the Python-based Flopy packages.[72] The transport model solves the advection-dispersion equation with a first-order irreversible deposition term (Equation 1, SI). The model was built to simulate bacteria transport in the same length column with a porosity $\phi = 0.39$ and dispersivity $\alpha = 0.13$ cm. The bulk column porosity and dispersivity were found by fitting an analytical model to the breakthrough curves of fluorescein dye tracer and bacteria in identical column experiments. Breakthrough curves in those experiments were obtained by measuring concentration using a UV-Vis spectrophotometer (*Shimadzu* UV-1900i). The ratio of the transverse dispersivity and the longitudinal dispersivity was assumed 1:10 (or 0.1) in the standard isotropic model.[73]

The model was discretized to identically match the PET image discretization. The initial

3D column shape was defined as a grid with 17 cells x 17 cells x 57 cells in the x-y-z direction, where xy plane is orthogonal to the long axis of the column. Similar to the PET images, each cell in the model had a dimension of 1.553 mm x 1.553 mm x 1.592 mm. The cylindrical shape of the column was preserved in the model by inactivating the cells outside the column geometry. A constant head (Dirichlet) boundary condition was applied at the outlet of the column. A constant flow rate condition equal to the experimental injection rate of 1.826 mL/min was applied as the inlet boundary condition. The initial condition was zero concentration at time t=0. Identical to the experiment, a 1 mL pulse of bacteria was injected and immediately displaced by solution with no bacteria or tracer.

The three-dimensional attachment coefficients measured from PET as described in the previous section were used to describe the attachment coefficient k_f in each corresponding grid cell of the model. The 3D model output was used to calculate bacterial attachment maps (S^*/C_0) based on the voxel-scale k_f and bacteria breakthrough curves using Equation 3 in the SI. This spatially-resolved attachment map calculated from the numerical model output was then compared with the attachment measured from the PET images. Results from the model were used to validate that the PET analysis method can directly quantify the k_f distribution in heterogeneous geologic column experiments. The full model input and output files are available in a repository provided in the Acknowledgements.

Results and Discussions

Validation of radiolabeling methodology for determination of bacterial transport and attachment

Batch experiments (SI, Figure S2) showed that approximately 82.5% of [^{18}F]-FDG was taken up by *E. coli* P8 grown in LB broth and suspended in 1 mM NaCl and an average of 81.4% of the radiolabeled was retained by the cells after resuspension in fresh saline solution (1 mM NaCl). The raw bacteria concentration data in the effluent samples (available in a

repository listed in the Acknowledgment) were used to generate the breakthrough curve in Figure S3. The amount of FDG in bacteria versus free solution in the column effluent collected 10 minutes after the start of pulse injection was ca. 83%, similar to the level of retention observed in batch experiments. Because virtually all unattached [^{18}F]-FDG labeled bacteria and free [^{18}F]-FDG were eluted from the column after 14 minutes (SI, Figure S3), any radioactivity remaining in the column at that time was assumed to be attached bacteria. These results confirm that the radiolabeling of the P8 cells with [^{18}F]-FDG was sufficiently stable to permit the determination of bacterial attachment in the column by PET analysis at 14 minutes after pulse injection. The small amount of radioactivity continuously present in the column effluent toward the end of the experiment (SI, Figure S3) can be attributed to a combination of free [^{18}F]-FDG released from attached bacteria, as well as a small amount of radiolabeled bacteria tailing in secondary minimum association with surfaces that were re-entrained into the bulk fluid. This release was minor, however, compared to the amount of radioactivity associated with the attached bacteria at the time of PET analysis. Collectively, these results confirm that our radiolabeling methodology was sufficient to enable the calculation of spatially-resolved bacterial transport and attachment in the column.

Three-dimensional quantification of bacteria transport in heterogeneous sand pack

Bacterial transport was quantified *in situ* using the voxel-scale concentration of radioactivity measured with PET in the sand-packed column. The normalized concentration of the radiotracer and radiolabeled bacteria throughout the columns as a function of time is shown in Figure 2. From these images, it is clear that the *E. coli* P8 pulse experienced greater apparent dispersion and substantial attachment during transport relative to the ^{18}F-FDG conservative radiotracer. Nonuniform plume shapes of both the tracer and bacteria at early timesteps (e.g. PV = 0.30) were driven by nonuniform fluid injection across the face of the inlet cap that inevitably arose at the transition from small diameter tubing to a larger diameter (2.54

cm) column. Some minor plume distortion was also driven by small-scale heterogeneity at the interfaces between the inlet and middle sand layers as illustrated in the X-ray CT image of the column (Figure 1, top). Overall, these time-course concentration maps from PET data provided dynamic spatially-resolved tracer and bacterial concentrations throughout the entire column over the course of the experiments. These data provided breakthrough curves at the voxel-scale that were used to calculate spatially-resolved attachment rate coefficients.

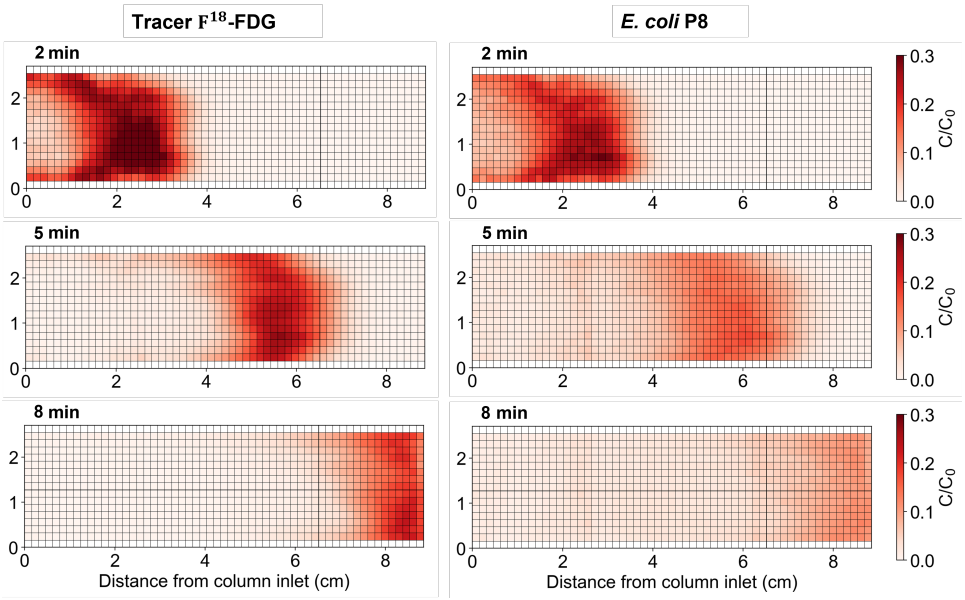

Figure 2: Two-dimensional slices from the 3D PET images showing time-course concentration (C/C_0) of the radiotracer ^{18}F-FDG (left) and radiolabeled P8 bacteria (right) during separate pulse injection experiments in the heterogeneous sand-packed column. Color scale indicates the normalized concentration that was averaged around the center longitudinal slice of the column. Each voxel size is 1.553 mm x 1.553 mm x 1.592 mm. PET concentration images are shown at 2, 5, and 8 minutes (PV = 0.30, 0.61, and 0.92, respectively) from the start of the pulse injection. This figure highlights the ability to resolve *in situ* time-lapse bacteria transport behavior with PET imaging.

Bacteria attachment distributions in layered sandpacks

Bacterial attachment and deposition rate coefficients were quantified from the PET data immediately after the bacteria pulse passed through the column. At approximately 14 minutes after the initiation of the bacterial pulse injection (PV = 1.53), the mobile bacteria had completely exited the column. After this time, the PET-measured radioactivity inside the

column represents the bacteria that were attached to the sand matrix (denoted as S^*/C_0). This inference was possible because of *E. coli* P8 stable retention of radiotracer over the course of 3.5 hours, well exceeding the column transport experiment duration (SI, Figure S2). The attached bacterial concentration (S^*/C_0) was also quantified at the voxel-scale level in the entire 3D column. Using these measurements of voxel-scale breakthrough curves and attached bacterial concentrations, the attachment coefficients (k_f) were directly calculated using Equation 4 in the SI. The breakthrough curves were voxel volume-averaged concentration of bacteria measured as a function of time.

The attachment coefficients averaged along the longitudinal slices of the column are shown in Figure 3 along with the one-dimensional profile of slice-average k_f. Probability density of k_f in each sand layer is plotted in Figure 4 for statistical comparison of the attachment distributions between layers and between experiments. More bacteria were attached in the middle M324 sand layer than in the inlet and outlet layers packed with M356 sand. As a result, both the inlet and outlet layers with M356 sand had similar modal values of $k_f = 0.020$ min^{-1}, which was smaller than modal $k_f = 0.035$ min^{-1} in the slightly finer M324 sand (Figure 4). However, the maximum concentration of attached bacteria was at the interfaces between the two sand types (located around 2-2.5 cm and 6.5 cm from the column inlet). Skewness towards higher k_f in the inlet layer k_f distribution shown in Figure 4 was due to the higher k_f values at the interfacial regions being included in the inlet layer. The attachment coefficients at the interfaces were at least twice as large as the modal k_f in both layers, ranging from 0.050 up to 0.090 min^{-1}. Compared with similar UV-Vis column experiments using non-concentrated and non-radiolabeled bacteria suspension, the k_f fitted from the spectrophotometric breakthrough curve fell within the range of the local k_f distributions measured from PET experiment. This agreement in the attachment coefficients indicates that the radioactive label [^{18}F]-FDG had negligible impact on the cell transport of *E. coli*. Earlier mean arrival time breakthrough of bacteria relative to the solute tracer in the UV-Vis experiment suggests that pore-size exclusion is likely in the PET experiments as has been

observed in other studies.[18,25,74,75]

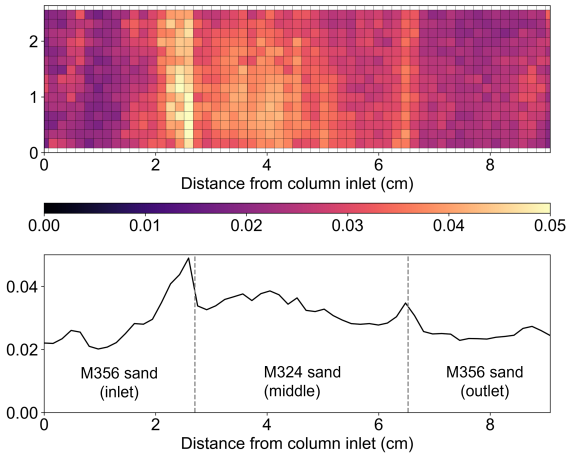

Figure 3: (Top) Two-dimensional distribution of attachment coefficients (k_f) averaged along the center longitudinal axis of the column after the bacterial pulse exited column at τ=14 min (PV = 1.53) since pulse injection. Each voxel size is 1.553 mm x 1.553 mm x 1.592 mm. (Bottom) One-dimensional slice-averaged k_f in the sand column. Higher attachment coefficients were observed at the interfaces between the sand layers (dashed lines), and finer M324 sand exhibited greater k_f values than M356 sand.

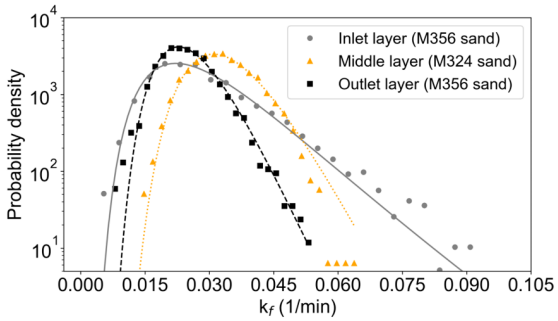

Figure 4: Probability density distributions of attachment coefficients (k_f) in each sand layer (solid points) fitted with lognormal distribution curves (lines). Inlet M356 sand layer had similar distribution to outlet M356 sand layer, albeit having a higher k_f tailing due to higher attachment at the interface. The finer M324 sand exhibited slightly higher range of k_f distribution than M356 sand.

Numerical model parameterization from PET data

The three-dimensional attachment coefficient distribution calculated from the PET images and shown in Figure 3 was incorporated into the 3D numerical model to calculate *E. coli* attachment in the heterogeneous column. The model-calculated bacterial attachment matched

closely with the experimental PET results as illustrated in both the 2D and 1D profiles in Figure 5. The 1D profiles show that the bacteria attached (S^*/C_0) at the coarse inlet and outlet layers ranged from 0.010 to 0.013, and was higher in the middle layer (S^*/C_0 = 0.012-0.017). More bacteria were attached at the interface near the inlet (S^*/C_0 = 0.015-0.025) than at the second interface down-gradient (S^*/C_0 = 0.010-0.016). A second simulation was conducted assuming a single k_f, which was determined from the average k_f of all the voxels calculated from PET results. The experimental PET data highlight variability in bacterial attachment as opposed to an exponential decrease in deposition with distance suggested by the homogeneous k_f model (Figure 5, top) and other bacterial transport studies in unfavorable conditions. These results highlight that k_f can be directly quantified *in situ* from PET data and can be described as a heterogeneous parameter field in a transport model. Under such heterogeneity, the first-order transport model with irreversible attachment closely reproduced the bacteria attachment behavior observed in the column experiments.

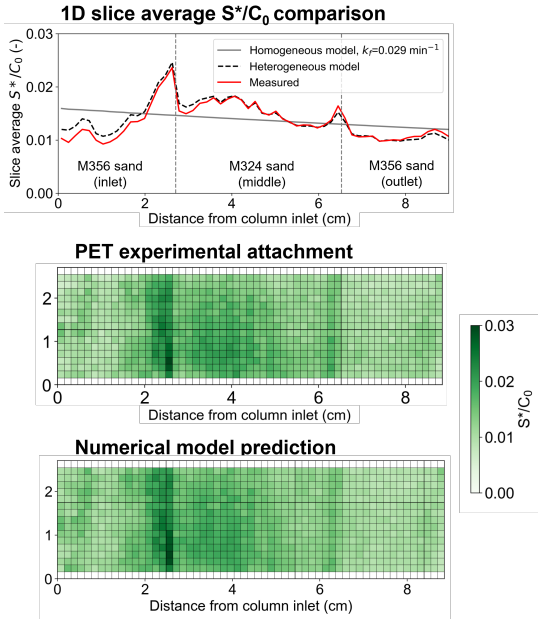

Figure 5: (Top) Comparison of the 1D slice-average bacterial attachment (S^*/C_0) between PET result and two numerical model predictions. The heterogeneous model was run based on the 3D heterogeneous k_f distribution measured from PET. The homogeneous model assumed a single $k_f = 0.029$ min^{-1} for the entire column, which was the average k_f value in all voxels of the column from PET measurement. (Middle and bottom) Two-dimensional slice-average S^*/C_0 maps for the numerical model and PET measured data, respectively. The voxel size in these maps is 1.553 mm x 1.553 mm x 1.592 mm. The predicted attachment from the heterogeneous model matched closely with the experiment PET result, indicating an accurate quantification of spatially-resolved bacteria attachment coefficients.

Discussion of calculated bacteria attachment

The attachment rate coefficients measured in this study are comparable with literature values in previous studies of bacteria transport in sand packs, but direct comparison is difficult due to differences in experimental conditions such as pore-water velocity, ionic strength (IS), pH, bacteria strain, injected bacteria mass, bacteria concentration, sand grain properties, and mineralogy. The average k_f results of 0.020 to 0.035 min^{-1} for M356 and M324 sands in Figure 3 were measured under an ionic strength (IS) of 1 mM NaCl, circumneutral pH, and flow rate Q=1.826 ml/min (pore-water velocity v_p= 0.924 cm/min). Previous studies based on experiments with similar IS, pH, grain size, and sand type have resulted in k_f values

that were similar (k_f = 0.0175-0.0238 min^{-1}),[76] two to three times lower (k_f =7.59×10^{-3} min^{-1}),[77] and almost 10 times lower (k_f= 3.68E-3 min^{-1})[48] than the values observed in Figure 3. However, these results were based on different flow rates, strains of *E. coli*, sand pack mineralogy, and different volumes and masses of injected bacteria. Given these differences, our experimental k_f results can be considered consistent with values found in the literature.

The higher experimental k_f found for M324 sand (finer) than M356 sand (coarser) is consistent with literature values but does not explain the observation of the highest attachment coefficients occurring at the interface between sand layers. Many studies have observed bacteria retention decreasing with increasing grain size,[23,78] as expected from colloid filtration theory. However, some studies have found that small grain size variation did not display significant impacts on bacteria attachment compared to other factors such as pore volumes of bacteria injected and pore size,[48,79] cell motility,[76,80,81] grain properties (surface area, angularity, roughness),[82] or metal oxide content.[83] Other bacteria deposition mechanisms such as aggregation, ripening, straining, and/or hydrodynamic bridging could contribute to the attachment behaviors observed;[48,78,84,85] however, direct attribution of these mechanisms to the observed pattern is not possible without corresponding pore-scale observations.

In this study, the porosity between M324 and M356 sands only differed by 1-3% and differences in grain size distribution were subtle (Figure 1). Despite these subtle differences, the observation of attachment differences at the interfaces illustrates the capability of PET imaging during column experiments in detecting small changes in bacteria concentration and attachment in subtly heterogeneous geologic materials with greater precision relative to other macroscale methods.

The presence of oxide minerals is a potential source of the higher attachment near the sand layer interfaces or spatial variation in the retention rate coefficients within the layers. Higher bacterial attachment is often observed with higher content of oxide minerals as a result of favorable attachment conditions. In particular, this behavior has been observed on oxyhydroxide-coated surfaces[83,86–91] as well as aluminum-coated sands.[86,92–97] The presence

of oxide minerals is also detected through the micro-CT image of sand M324 as white grains with higher X-ray attenuation in Figure 1. However, variation in volumetric oxide content is not significant enough to be quantified or visualized with X-ray CT in the column scale. Thus, oxide minerals remain the potential cause of greater colloid deposition at the sand interfaces. Studying the influence of spatially variable oxide content on bacterial attachment using PET imaging is an area of future work.

A likely mechanism for higher attachment at the sand layer interfaces is that these areas are local transitional regions in pore-scale velocity distribution and where local porosity could be reduced due to potential packing differences. Packing and/or differences in grain size may have also contributed to increasing pore-scale complexity which has been observed to widen pore-water velocity distributions[98–101] and could lead to more colloids reaching the grain surface based on previous pore-scale simulation studies.[79,102–105] Under unfavorable attachment conditions, bacteria attachment is largely driven by local variations in velocity. This has been observed in experiments and models at grain-grain contacts,[48] near grain surfaces where roughness leads to enhanced attachment,[15,106] and regions of decreasing pore water velocity.[79,82,107–110]

Implications

While bacterial radiolabeling with [^{18}F]-FDG for use in PET imaging has been investigated in the clinical settings,[63] geoscientific application of PET has been limited to monitoring flow and transport in porous and fractured media.[111–115] In this study, the combination of radiolabeling *E. coli* with positron-emitting radioisotopes and imaging the dynamic 3D *E. coli* distributions in heterogeneous sand-packed columns provides measurements of *in situ* bacteria transport and attachment in geologic materials at the Darcy scale. This radiolabeling and imaging approach enables the direct quantification of spatially-variable bacteria attachment coefficients in heterogeneous geologic media. Consistent with other studies, higher *E. coli*

P8 attachment was observed in the slightly finer M324 sand compared to the M356 sands despite the minor difference in porosity and grain size distribution. The highest bacteria attachment was observed at the interfaces between the different sand layers, highlighting the importance of studying bacteria transport in nonideal geologic media.

The demonstrated ability of the 3D model—parameterized with the measured attachment distributions—to reproduce the experimental results suggests that with more measurements across different geological media and environmental conditions, it may be possible to describe fundamental attachment rate coefficient information (e.g. PDFs) in a process-based framework. Overall, the bacterial radiolabeling and PET imaging technique is applicable in geologic media and soils to enable transport studies under more realistic conditions. Understanding the role of different processes and geologic conditions on attachment rate distributions could enable more accurate bacteria transport and attachment prediction in geologic systems at larger scales.

Acknowledgement

The Python scripts for analysis, model development, and generation of Figures 2-5 and Figures S2 and S3 in the SI are available at https://doi.org/10.5281/zenodo.7659168.

This work was supported by the University of Wisconsin Water Resources Institute under Grant Number WR21R001. The experimental system used for column and imaging experiments was supported by the National Science Foundation under Grant No. 2002412. Any opinions, findings, and conclusions or recommendations expressed in this material are those of the authors and do not necessarily reflect the views of the National Science Foundation. The authors would like to acknowledge the Cancer Center Support Grant: NCI P30 CA014520 and the University of Wisconsin Small Animal Imaging & Radiotherapy Facility for supporting the imaging resources used in this work. Additional support for this work was provided by the Office of the Vice Chancellor for Research and Graduate Education

at the University of Wisconsin-Madison with funding from the Wisconsin Alumni Research Foundation. The authors would like to thank Justin Jeffery for assistance with the PET and CT imaging and Michael Thomas and Reinier Hernandez for assistance with experimental protocols. We thank Chris Massey and Collin Sutton for their experimental assistance.

Supporting Information Available

This Supporting Information is available free of charge at http://pubs.acs.org. Supporting Information: Column preparation and PET imaging experiment, bacteria growth methodology, bacteria uptake and retention experimental verification, confirmation of radiolabeling stability through bacteria breakthrough curves during PET experiment, measurement of the stability of the cell suspension, and derivations of the attachment coefficient calculation from PET images.

References

(1) Bradford, S.; Torkzaban, S. Colloid Transport and Retention in Unsaturated Porous Media: A Review of Interface-, Collector-, and Pore-Scale Processes and Models. *Vadose Zone Journal* **2008**, *7*, 667–681.

(2) Bradford, S.; Segal, E. Fate of Indicator Microorganisms Under Nutrient Management Plan Conditions. *Journal of Environmental Quality* **2009**, *38*, 1728–1738.

(3) Wu, S.; Luo, Y.; Cheung, K.; Wong, M. Influence of bacteria on Pb and Zn speciation, mobility and bioavailability in soil: A laboratory study. *Environmental Pollution* **2006**, *144*, 765–773.

(4) Kim, H.; Jaffé, P. Spatial distribution and physiological state of bacteria in a sand column experiment during the biodegradation of toluene. *Water Research* **2007**, *41*, 2089–2100.

(5) Nilsso, C.; Lakshmanan, R.; Renman, G.; Rajarao, G. Efficacy of reactive mineral-based sorbents for phosphate, bacteria, nitrogen and TOC removal – Column experiment in recirculation batch mode. *Water Research* **2013**, *47*, 5165–5175.

(6) Duffy, G. Verocytoxigenic Escherichia coli in animal faeces, manures and slurries. *Journal of Applied Microbiology* **2003**, *94*, 94–103.

(7) Shere, J.; Bartlett, K.; ; Kaspar, C. Longitudinal Study of Escherichia coli O157:H7 Dissemination on Four Dairy Farms in Wisconsin. *Applied and Environmental Microbiology* **1998**, *64*, 1390–1399.

(8) Zhao, T.; Doyle, M.; Shere, J.; Garber, L. Prevalence of enterohemorrhagic Escherichia coli O157:H7 in a survey of dairy herds. *Applied and Environmental Microbiology* **1995**, *61*, 1290–1293.

(9) Hutchison, M.; Walters, L.; Moore, T.; Thomas, D.; Avery, S. Fate of Pathogens Present in Livestock Wastes Spread onto Fescue Plots. *Applied and Environmental Microbiology* **2005**, *71*, 691–696.

(10) Jones, P. In *Sewage sludge as a vector of Salmonellosis*; Block, J., Havelaar, A., L'Hermite, P., Eds.; Elsevier Applied Science, 1986; pp 21–33.

(11) Happel, J. Viscous flow in multiparticle systems: Slow motion of fluids relative to beds of spherical particles. *AIChE Journal* **1958**, *4*, 197–201.

(12) Yao, K.; Habibian, M.; O'Melia, C. Water and waste water filtration: Concepts and applications. *Environmental Science and Technology* **1971**, *5*, 1105–1112.

(13) Rajagopalan, R.; Tien, C. Trajectory analysis of deep-bed filtration with the sphere-in-cell porous media model. *AIChE Journal* **1976**, *22*, 523–533.

(14) Torkzaban, S.; Bradford, S. A.; Walker, S. L. Resolving the coupled effects of hydrodynamics and DLVO forces on colloid attachment in porous media. *Langmuir* **2007**, *23*, 9652–9660.

(15) Johnson, W. P.; Hilpert, M. Upscaling colloid transport and retention under unfavorable conditions: Linking mass transfer to pore and grain topology. *Water Resources Research* **2013**, *49*, 5328–5341.

(16) Johnson, W. P.; Rasmuson, A.; Pazmiño, E.; Hilpert, M. Why Variant Colloid Transport Behaviors Emerge among Identical Individuals in Porous Media When Colloid-Surface Repulsion Exists. *Environmental Science and Technology* **2018**, *52*, 7230–7239.

(17) Rowthu, S.; Hoffmann, P. *Versatile micro- and nanotexturing techniques for antibacterial applications*; Elsevier, 2019; pp 27–62.

(18) Sirivithayapakorn, S.; Keller, A. Transport of colloids in saturated porous media: A pore-scale observation of the size exclusion effect and colloid acceleration. *Water Resources Research* **2003**, *39*.

(19) Bradford, S. A.; Simunek, J.; Bettahar, M.; Van Genuchten, M. T.; Yates, S. R. Modeling colloid attachment, straining, and exclusion in saturated porous media. *Environmental Science and Technology* **2003**, *37*, 2242–2250.

(20) Chrysikopoulos, C. V.; Katzourakis, V. E. Colloid particle size-dependent dispersivity. *Water Resources Research* **2015**, *51*, 4668–4683.

(21) Tufenkji, N.; Elimelech, M. Breakdown of colloid filtration theory: Role of the secondary energy minimum and surface charge heterogeneities. *Langmuir* **2005**, *21*, 841–852.

(22) Li, X.; Scheibe, T. D.; Johnson, W. P. Apparent decreases in colloid deposition rate coefficients with distance of transport under unfavorable deposition conditions: A general phenomenon. *Environmental Science and Technology* **2004**, *38*, 5616–5625.

(23) Kim, H. N.; Walker, S. L.; Bradford, S. A. Coupled factors influencing the transport and retention of Cryptosporidium parvum oocysts in saturated porous media. *Water Research* **2010**, *44*, 1213–1223.

(24) Grolimund, D.; Elimelech, M.; Borkovec, M.; Barmettler, K.; Kretzschmar, R.; Sticher, H. Transport of in situ mobilized colloidal particles in packed soil columns. *Environmental Science and Technology* **1998**, *32*, 3562–3569.

(25) Keller, A. A.; Sirivithayapakorn, S.; Chrysikopoulos, C. V. Early breakthrough of colloids and bacteriophage MS2 in a water-saturated sand column. *Water Resources Research* **2004**, *40*, W08304.

(26) Johnson, W. P.; Blue, K. A.; Logan, B. E.; Arnold, R. G. Modeling Bacterial Detachment During Transport Through Porous Media as a Residence-Time-Dependent Process. *Water Resources Research* **1995**, *31*, 2649–2658.

(27) Bradford, S. A.; Toride, N. A stochastic model for colloid transport and deposition. *Journal of Environmental Quality* **2007**, *36*, 1346–1356.

(28) Duffy, K. J.; Cummings, P. T.; Ford, R. M. Random walk calculations for bacterial migration in porous media. *Biophysical Journal* **1995**, *68*, 800–806.

(29) Zhang, P.; Johnson, W. P.; Scheibe, T. D.; Choi, K.-h.; Dobbs, F. C.; Mailloux, B. J. Extended tailing of bacteria following breakthrough at the Narrow Channel Focus Area, Oyster, Virginia. *Water Resources Research* **2001**, *37*, 2687–2698.

(30) Scheibe, T. D.; Wood, B. D. A particle-based model of size or anion exclusion with

application to microbial transport in porous media. *Water Resources Research* **2003**, *39*, 1–10.

(31) Li, X.; Johnson, W. P. Nonmonotonic variations in deposition rate coefficients of microspheres in porous media under unfavorable deposition conditions. *Environmental Science and Technology* **2005**, *39*, 1658–1665.

(32) Tong, M.; Camesano, T. A.; Johnson, W. P. Spatial variation in deposition rate coefficients of an adhesion-deficient bacterial strain in quartz sand. *Environmental Science and Technology* **2005**, *39*, 3679–3687.

(33) VanNess, K.; Rasmuson, A.; Ron, C. A.; Johnson, W. P. A Unified Force and Torque Balance for Colloid Transport: Predicting Attachment and Mobilization under Favorable and Unfavorable Conditions. *Langmuir* **2019**, *35*, 9061–9070.

(34) Harvey, R. W.; Kinner, N. E.; Bunn, A.; MacDonald, D.; Metge, D. Transport behavior of groundwater protozoa and protozoan-sized microspheres in sandy aquifer sediments. *Applied and Environmental Microbiology* **1995**, *61*, 209–217.

(35) Silliman, S. E.; Dunlap, R.; Fletcher, M.; Schneegurt, M. A. Bacterial transport in heterogeneous porous media: Observations from laboratory experiments. *Water Resources Research* **2001**, *37*, 2699–2707.

(36) Bradford, S. A.; Bettahar, M.; Simunek, J.; van Genuchten, M. T. Straining and Attachment of Colloids in Physically Heterogeneous Porous Media. *Vadose Zone Journal* **2004**, *3*, 384–394.

(37) Johnson, W. P. Quantitative Linking of Nanoscale Interactions to Continuum-Scale Nanoparticle and Microplastic Transport in Environmental Granular Media. *Environmental Science Technology* **2020**, *54*, 8032–8042.

519 (38) Yoon, J. S.; Germaine, J. T.; Culligan, P. J. Visualization of particle behavior within a
520 porous medium: Mechanisms for particle filtration and retardation during downward
521 transport. *Water Resources Research* **2006**, *42*, 1–16.

522 (39) Tufenkji, N.; Redman, J. A.; Elimelech, M. Interpreting Deposition Patterns of Mi-
523 crobial Particles in Laboratory-Scale Column Experiments. *Environmental Science*
524 *Technology* **2003**, *37*, 616–623.

525 (40) Raychoudhury, T.; Tufenkji, N.; Ghoshal, S. Straining of polyelectrolyte-stabilized
526 nanoscale zero valent iron particles during transport through granular porous media.
527 *Water Research* **2014**, *50*, 80–89.

528 (41) Matthew Thomas, J.; Chrysikopoulos, C. V. A new method for in situ concentration
529 measurements in packed-column transport experiments. *Chemical Engineering Science*
530 **2010**, *65*, 4285–4292.

531 (42) Molnar, I. L.; Willson, C. S.; O'Carroll, D. M.; Rivers, M. L.; Gerhard, J. I. Method for
532 obtaining silver nanoparticle concentrations within a porous medium via synchrotron
533 X-ray computed microtomography. *Environmental Science and Technology* **2014**, *48*,
534 1114–1122.

535 (43) Gaillard, J. F.; Chen, C.; Stonedahl, S. H.; Lau, B. L.; Keane, D. T.; Packman, A. I.
536 Imaging of colloidal deposits in granular porous media by X-ray difference micro-
537 tomography. *Geophysical Research Letters* **2007**, *34*, 2–6.

538 (44) Perez, A. J.; Patiño, J. E.; Soos, M.; Morales, V. L. Morphology of Shear-Induced
539 Colloidal Aggregates in Porous Media: Consequences for Transport, Deposition, and
540 Re-entrainment. *Environmental Science and Technology* **2020**, *54*, 5813–5821.

541 (45) Olson, M. S.; Ford, R. M.; Smith, J. A.; Fernandez, E. J. Quantification of bacterial
542 chemotaxis in porous media using magnetic resonance imaging. *Environmental Science*
543 *and Technology* **2004**, *38*, 3864–3870.

(46) Sherwood, J. L.; Sung, J. C.; Ford, R. M.; Fenandez, E. J.; Maneval, J. E.; Smith, J. A. Analysis of bacterial random motility in a porous medium using magnetic resonance imaging and immunomagnetic labeling. *Environmental Science and Technology* **2003**, *37*, 781–785.

(47) Baumann, T.; Werth, C. J. Visualization of colloid transport through heterogeneous porous media using magnetic resonance imaging. *Colloids and Surfaces A: Physicochemical and Engineering Aspects* **2005**, *265*, 2–10.

(48) Bradford, S. A.; Simunek, J.; Walker, S. L. Transport and straining of E. coli O157:H7 in saturated porous media. *Water Resources Research* **2006**, *42*, 1–12.

(49) Toran, L.; Palumbo, A. Colloid transport through fractured and unfractured laboratory sand columns. *Journal of Contaminant Hydrology* **1992**, *9*, 289–303.

(50) Redman, J. A.; Walker, S. L.; Elimelech, M. Bacterial Adhesion and Transport in Porous Media: Role of the Secondary Energy Minimum. *Environmental Science and Technology* **2004**, *38*, 1777–1785.

(51) Han, P.; Shen, X.; Yang, H.; Kim, H.; Tong, M. Influence of nutrient conditions on the transport of bacteria in saturated porous media. *Colloids and Surfaces B: Biointerfaces* **2013**, *102*, 752–758.

(52) Qu, D.; Ren, H.; Zhou, R.; Zhao, Y. Visualisation study on Pseudomonas migulae AN-1 transport in saturated porous media. *Water Research* **2017**, *122*, 329–336.

(53) Levin, C. In *Emission Tomography: The Fundamentals of PET and SPECT*; Wernick, M. N., Aarsvold, J. N., Eds.; Elsevier, 2004; Vol. 5; Chapter Chapter 4, pp 53–88.

(54) Zahasky, C.; Benson, S. M. Micro-Positron Emission Tomography for Measuring Sub-

core Scale Single and Multiphase Transport Parameters in Porous Media. *Advances in Water Resources* **2018**, *115*, 1–16.

(55) Zahasky, C.; Kurotori, T.; Pini, R.; Benson, S. M. Positron emission tomography in water resources and subsurface energy resources engineering research. *Advances in Water Resources* **2019**, *127*, 39–52.

(56) Goscinski, N. Investigation of 89Zr-Siderophores as Molecular Imaging Agents for Positron Emission Tomography Imaging of Bacterial Infections. **2015**, 51–61.

(57) Petrik, M.; Zhai, C.; Novy, Z.; Urbanek, L.; Haas, H.; Decristoforo, C. In Vitro and In Vivo Comparison of Selected Ga-68 and Zr-89 Labelled Siderophores. *Molecular Imaging and Biology* **2016**, *18*, 344–352.

(58) Petrik, M.; Zhai, C.; Haas, H.; Decristoforo, C. Siderophores for molecular imaging applications. *Clinical and Translational Imaging* **2017**, *5*, 15–27.

(59) M.Miethke,; Marahiel, M. Siderophore-Based Iron Acquisition and Pathogen Control. *Microbiology and Molecular Biology Reviews* **2007**, *71*, 413–451.

(60) Koh, E.; Henderson, J. Microbial Copper-binding Siderophores at the Host-Pathogen Interface. *Journal of Biological Chemistry* **2015**, *290*, 18967–18974.

(61) Siddiqui, N.; Houson, H.; Thomas, S.; Blanco, J.; O'donnell, R.; Hassett, D.; Lapi, S.; Kotagiri, N. Radiolabelled Bacterial Metallophores as Targeted PET Imaging Contrast Agents for Accurate Identification of Bacteria and Outer Membrane Vesicles in vivo. **2020**, 1–32.

(62) Yu, S. Review of 18F-FDG synthesis and quality control. *Biomedical Imaging and Intervention Journal* **2006**, *2*, e57.

(63) Heuker, M.; Sijbesma, J. W.; Suárez, R. A.; Jong, J. R. D.; Boersma, H. H.; Luurtsema, G.; Elsinga, P. H.; Glaudemans, A. W.; Dam, G. M. V.; Dijl, J. M. V.;

Slart, R. H.; Oosten, M. V. In vitro imaging of bacteria using 18F-fluorodeoxyglucose micro positron emission tomography. *Scientific Reports* **2017**, *7*, 1–9.

(64) Niebuhr S. E.; Laury, G. R., A.; Acuff; Dickson, J. S. Evaluation of Nonpathogenic Surrogate Bacteria as Process Validation Indicators for Salmonella enterica for Selected Antimicrobial Treatments, Cold Storage, and Fermentation in Meat. *Journal of Food Protection* **2008**, *71*, 714–718.

(65) Marshall, S. E. A. G. R., K. M.; Niebuhr; Lucia, L. M.; Dickson, J. S. Identification of Escherichia coli O157:H7 Meat Processing Indicators for Fresh Meat through Comparison of the Effects of Selected Antimicrobial Interventions. *Journal of Food Protection* **2005**, *68*, 2580–2586.

(66) Keeling, S. E. A. G. R., C.; Niebuhr; Dickson, J. S. Evaluation of Escherichia coli Biotype I as a Surrogate for Escherichia coli O157:H7 for Cooking, Fermentation, Freezing, and Refrigerated Storage in Meat Processes. *Journal of Food Protection* **2009**, *72*, 728–732.

(67) Cabrer-Diaz, T. M. L. L. M. D. J. S. C. A., E.; Moseley; Acuff, G. R. Fluorescent Protein–Marked Escherichia coli Biotype I Strains as Surrogates for Enteric Pathogens in Validation of Beef Carcass Interventions. *Journal of Food Protection* **2009**, *72*, 295–303.

(68) Chen, C.-Y.; Nace, G. W.; Irwin, P. L. A 6×6 drop plate method for simultaneous colony counting and MPN enumeration of Campylobacter jejuni, Listeria monocytogenes, and Escherichia coli. *Journal of Microbiological Methods* **2003**, *55*, 475–479.

(69) Kurotori, T.; Zahasky, C.; Hosseinzadeh Hejazi, S. A.; Shah, S. M.; Benson, S. M.; Pini, R. Measuring, imaging and modelling solute transport in a microporous limestone. *Chemical Engineering Science* **2019**, *196*, 366–383.

(70) Harbaugh, A. W. *MODFLOW-2005, the U.S. Geological Survey modular groundwater model - the groundwater flow process*; 2005.

(71) Zheng, C.; Wang, P. P. MT3DMS - A Modular Three-Dimensional Multispecies Transport Model. *Strategic Environmental Research and Development Program* **1999**, 1–40.

(72) Bakker, M.; Post, V.; Langevin, C. D.; Hughes, J. D.; White, J. T.; Starn, J. J.; Fienen, M. N. Scripting MODFLOW Model Development Using Python and FloPy. *Groundwater* **2016**, *54*, 733–739.

(73) flopy Documentation - Release 3.3.3, year = 2021, url =.

(74) Chrysikopoulos, C. V.; Abdel-Salam, A. Modeling colloid transport and deposition in saturated fractures. *Colloids and Surfaces A: Physicochemical and Engineering Aspects* **1997**, *121*, 189–202.

(75) Dong, H.; Onstott, T. C.; DeFlaun, M. F.; Fuller, M. E.; Scheibe, T. D.; Streger, S. H.; Rothmel, R. K.; Mailloux, B. J. Relative Dominance of Physical versus Chemical Effects on the Transport of Adhesion-Deficient Bacteria in Intact Cores from South Oyster, Virginia. *Environmental Science Technology* **2002**, *36*, 891–900.

(76) Bai, H.; Cochet, N.; Pauss, A.; Lamy, E. Bacteria cell properties and grain size impact on bacteria transport and deposition in porous media. *Colloids and Surfaces B: Biointerfaces* **2016**, *139*, 148–155.

(77) Park, S.-J.; Lee, C.-G.; Kim, S.-B. Quantification of Bacterial Attachment-related Parameters in Porous Media. *Environmental Engineering Research* **2008**, *13*, 141–146.

(78) Bradford, S. A.; Simunek, J.; Bettahar, M.; Tadassa, Y. F.; Van Genuchten, M. T.; Yates, S. R. Straining of colloids at textural interfaces. *Water Resources Research* **2005**, *41*, 1–18.

(79) Hemmatian, T.; Lee, H.; Kim, J. Bacteria Adhesion of Textiles Influenced by Wettability and Pore Characteristics of Fibrous Substrates. *Polymers* **2021**, *13*, 223.

(80) Ford, R. M.; Harvey, R. W. Role of chemotaxis in the transport of bacteria through saturated porous media. *Advances in Water Resources* **2007**, *30*, 1608–1617.

(81) Tecon, R.; Or, D. Bacterial flagellar motility on hydrated rough surfaces controlled by aqueous film thickness and connectedness. *Scientific Reports* **2016**, *6*, 19409.

(82) Syngouna, V. I.; Chrysikopoulos, C. V. Transport of biocolloids in water saturated columns packed with sand: Effect of grain size and pore water velocity. *Journal of Contaminant Hydrology* **2012**, *129-130*, 11–24.

(83) Bolster, C. H.; Mills, A. L.; Hornberger, G. M.; Herman, J. S. Effect of surface coatings, grain size, and ionic strength on the maximum attainable coverage of bacteria on sand surfaces. *Journal of Contaminant Hydrology* **2001**, *50*, 287–305.

(84) Bradford, S. A.; Torkzaban, S.; Walker, S. L. Coupling of physical and chemical mechanisms of colloid straining in saturated porous media. *Water Research* **2007**, *41*, 3012–3024.

(85) Yang, H.; Balhoff, M. T. Pore-network modeling of particle retention in porous media. *AIChE Journal* **2017**, *63*, 3118–3131.

(86) Scholl, M. A.; Harvey, R. W. Laboratory investigations on the role of sediment surface and groundwater chemistry in transport of bacteria through a contaminated sandy aquifer. *Environmental Science Technology* **1992**, *26*, 1410–1417.

(87) Mills, A. L.; Herman, J. S.; Hornberger, G. M.; DeJesús, T. H. Effect of Solution Ionic Strength and Iron Coatings on Mineral Grains on the Sorption of Bacterial Cells to Quartz Sand. *Applied and Environmental Microbiology* **1994**, *60*, 3300–3306.

(88) Knapp, E. P.; Herman, J. S.; Hornberger, G. M.; Mills, A. L. The effect of distribution of iron-oxyhydroxide grain coatings on the transport of bacterial cells in porous media. *Environmental Geology* **1998**, *33*, 243–248.

(89) Becker, M. W.; Collins, S. A.; Metge, D. W.; Harvey, R. W.; Shapiro, A. M. Effect of cell physicochemical characteristics and motility on bacterial transport in groundwater. *Journal of Contaminant Hydrology* **2004**, *69*, 195–213.

(90) Bolster, C. H.; Cook, K. L.; Marcus, I. M.; Haznedaroglu, B. Z.; Walker, S. L. Correlating Transport Behavior with Cell Properties for Eight Porcine ¡i¿Escherichia coli¡/i¿ Isolates. *Environmental Science Technology* **2010**, *44*, 5008–5014.

(91) Kim, S.-B.; Park, S.-J.; Lee, C.-G.; Choi, N.-C.; Kim, D.-J. Bacteria transport through goethite-coated sand: Effects of solution pH and coated sand content. *Colloids and Surfaces B: Biointerfaces* **2008**, *63*, 236–242.

(92) Lee, C.-G.; Park, S.-J.; Han, Y.-U.; Park, J.-A.; Kim, S.-B. Bacterial Attachment and Detachment in Aluminum-Coated Quartz Sand in Response to Ionic Strength Change. *Water Environment Research* **2010**, *82*, 499–505.

(93) Kim, S.-B.; Park, S.-J.; Lee, C.-G.; Kim, H.-C. Transport and retention of ¡i¿Escherichia coli¡/i¿ in a mixture of quartz, Al-coated and Fe-coated sands. *Hydrological Processes* **2008**, *22*, 3856–3863.

(94) Morrow, J. B.; Stratton, R.; Yang, H.-H.; Smets, B. F.; Grasso, D. Macro- and Nanoscale Observations of Adhesive Behavior for Several ¡i¿E. coli¡/i¿ Strains (O157:H7 and Environmental Isolates) on Mineral Surfaces. *Environmental Science Technology* **2005**, *39*, 6395–6404.

(95) Truesdail, S.; Lukasik, J.; Farrah, S.; Shah, D.; Dickinson, R. Analysis of Bacterial Deposition on Metal (Hydr)oxide-Coated Sand Filter Media. *Journal of Colloid and Interface Science* **1998**, *203*, 369–378.

(96) Chen, J.; Truesdail, S.; Lu, F.; Zhan, G.; Belvin, C.; Koopman, B.; Farrah, S.; Shah, D. Long-term evaluation of aluminum hydroxide-coated sand for removal of bacteria from wastewater. *Water Research* **1998**, *32*, 2171–2179.

(97) Lukasik, J.; Cheng, Y.-F.; Lu, F.; Tamplin, M.; Farrah, S. R. Removal of microorganisms from water by columns containing sand coated with ferric and aluminum hydroxides. *Water Research* **1999**, *33*, 769–777.

(98) Bijeljic, B.; Raeini, A.; Mostaghimi, P.; Blunt, M. J. Predictions of non-Fickian solute transport in different classes of porous media using direct simulation on pore-scale images. *Physical Review E* **2013**, *87*, 013011.

(99) Datta, S. S.; Chiang, H.; Ramakrishnan, T. S.; Weitz, D. A. Spatial Fluctuations of Fluid Velocities in Flow through a Three-Dimensional Porous Medium. *Physical Review Letters* **2013**, *111*, 064501.

(100) Matyka, M.; Gołembiewski, J.; Koza, Z. Power-exponential velocity distributions in disordered porous media. *Physical Review E* **2016**, *93*, 013110.

(101) Meyer, D. W.; Bijeljic, B. Pore-scale dispersion: Bridging the gap between microscopic pore structure and the emerging macroscopic transport behavior. *Physical Review E* **2016**, *94*, 013107.

(102) Pazmino, E. F.; Ma, H.; Johnson, W. P. Applicability of Colloid Filtration Theory in Size-Distributed, Reduced Porosity, Granular Media in the Absence of Energy Barriers. *Environmental Science Technology* **2011**, *45*, 10401–10407.

(103) Zhang, M.; He, L.; Jin, X.; Bai, F.; Tong, M.; Ni, J. Flagella and Their Properties Affect the Transport and Deposition Behaviors of ¡i¿Escherichia coli¡/i¿ in Quartz Sand. *Environmental Science Technology* **2021**, *55*, 4964–4973.

(104) Lin, D.; Hu, L.; Bradford, S. A.; Zhang, X.; Lo, I. M. Pore-network modeling of colloid transport and retention considering surface deposition, hydrodynamic bridging, and straining. *Journal of Hydrology* **2021**, *603*, 127020.

(105) Lin, D.; Hu, L.; Bradford, S. A.; Zhang, X.; Lo, I. M. Prediction of collector contact efficiency for colloid transport in porous media using Pore-Network and Neural-Network models. *Separation and Purification Technology* **2022**, *290*, 120846.

(106) Rasmuson, A.; VanNess, K.; Ron, C. A.; Johnson, W. P. Hydrodynamic versus Surface Interaction Impacts of Roughness in Closing the Gap between Favorable and Unfavorable Colloid Transport Conditions. *Environmental Science Technology* **2019**, *53*, 2450–2459.

(107) Cushing, R. S.; Lawler, D. F. Depth Filtration: Fundamental Investigation through Three-Dimensional Trajectory Analysis. *Environmental Science Technology* **1998**, *32*, 3793–3801.

(108) Baumann, T.; Werth, C. J. Visualization and Modeling of Polystyrol Colloid Transport in a Silicon Micromodel. *Vadose Zone Journal* **2004**, *3*, 434–443.

(109) Li, X.; Zhang, P.; Lin, C. L.; Johnson, W. P. Role of Hydrodynamic Drag on Microsphere Deposition and Re-entrainment in Porous Media under Unfavorable Conditions. *Environmental Science Technology* **2005**, *39*, 4012–4020.

(110) Chen, J.; Yang, L.; Chen, X.; Ripp, S.; Zhuang, J. Coupled Effects of Pore Water Velocity and Soil Heterogeneity on Bacterial Transport: Intact vs. Repacked Soils. *Frontiers in Microbiology* **2022**, *13*.

(111) Pini, R.; Vandehey, N. T.; Druhan, J.; Neil, J. P. O.; Benson, S. M. Quantifying solute spreading and mixing in reservoir rocks using 3D PET imaging. *Journal of Fluid Mechanics* **2016**, *796*, 558–587.

(112) Kulenkampff, J.; Sto, M.; Gründig, M.; Manse, A.; Lippmann-pipke, J.; Kersten, M. Time-lapse 3D imaging by positron emission tomography of Cu mobilized in a soil column by the herbicide MCPA. *Scientific Reports* **2018**, *8*, 1–9.

(113) Zahasky, C.; Thomas, D.; Matter, J.; Maher, K.; Benson, S. M. Multimodal imaging and stochastic percolation simulation for improved quantification of effective porosity and surface area in vesicular basalt. *Advances in Water Resources* **2018**, *121*, 235–244.

(114) Zahasky, C.; Benson, S. M. Preferential Solute Transport in Low Permeability Zones During Spontaneous Imbibition in Heterogeneous Porous Media. *Water Resources Research* **2022**, *58*.

(115) Huang, Z.; Kurotori, T.; Pini, R.; Benson, S. M.; Zahasky, C. Three-Dimensional Permeability Inversion Using Convolutional Neural Networks and Positron Emission Tomography. *Water Resources Research* **2022**, *58*, 1–21.